



**HAL**  
open science

# Determining the soil-water retention curve using mercury intrusion porosimetry test in consideration of soil volume change

Wen-Jing Sun, Yu-Jun Cui

► **To cite this version:**

Wen-Jing Sun, Yu-Jun Cui. Determining the soil-water retention curve using mercury intrusion porosimetry test in consideration of soil volume change. *Journal of Rock Mechanics and Geotechnical Engineering*, 2020, 12 (5), pp.1070-1079. 10.1016/j.jrmge.2019.12.022 . hal-03045836

**HAL Id: hal-03045836**

**<https://enpc.hal.science/hal-03045836>**

Submitted on 17 Oct 2022

**HAL** is a multi-disciplinary open access archive for the deposit and dissemination of scientific research documents, whether they are published or not. The documents may come from teaching and research institutions in France or abroad, or from public or private research centers.

L'archive ouverte pluridisciplinaire **HAL**, est destinée au dépôt et à la diffusion de documents scientifiques de niveau recherche, publiés ou non, émanant des établissements d'enseignement et de recherche français ou étrangers, des laboratoires publics ou privés.



Distributed under a Creative Commons Attribution - NonCommercial 4.0 International License



22 **Abstract:**

23 There is close link between soil water retention curve and pore size distribution.  
24 Theoretically, mercury intrusion porosimetry (MIP) test simulates a soil drying path  
25 and the soil water retention curve  $SWRC_{MIP}$  can be deduced from the MIP results.  
26 However,  $SWRC_{MIP}$  does not include the volume change effect, as opposed to the  
27 [conventional SWRC which is directly determined by suction measurement or suction](#)  
28 [control techniques](#). Therefore, for deformable soils, there is significant difference  
29 between SWRC and  $SWRC_{MIP}$ . In this study, drying test was carried out on a  
30 reconstituted silty soil, and the volume change, suction and pore size distribution (PSD)  
31 were determined on samples at different water contents. [The change of the deduced](#)  
32 [SWRC<sub>MIP</sub> and its](#) relation with the conventional SWRC were analyzed, showing that the  
33 volume change of soil is the main reason for the difference between the conventional  
34 SWRC and the  $SWRC_{MIP}$ . Furthermore, based on the test results, a transformation  
35 model was proposed for SWRC and  $SWRC_{MIP}$ , by taking [the soil state with no longer](#)  
36 [volume change](#) as a reference. Comparison between the experimental and predicted  
37 SWRCs showed that the proposed model can satisfactorily consider the influence of  
38 soil volume change on its water retention property.

39

40 **Key words:** Soil-water retention curve; mercury intrusion porosimetry; transform;  $S_r$ -  
41  $s-e$  plot; deformable soils

42

43

44

## 45 1. INTRODUCTION

46

47 A soil-water retention curve (SWRC) describes the amount of soil water (in terms of  
48 gravimetric water content  $w$  or volumetric water content  $\vartheta$  or degree of saturation  $S_r$ )  
49 at a given suction  $s$ . This curve is essential in analysing water transfer in unsaturated  
50 soils. This curve is also of paramount importance when modelling the coupled hydro-  
51 mechanical behaviour of unsaturated soils (Wheeler, 1996; Sun et al., 2007; Nuth and  
52 Laloui, 2008; Sun and Sun, 2012).

53

54 Conventional SWRC are usually investigated using either suction measurement or  
55 suction control techniques. However, application of these techniques is usually time  
56 consuming (Aubertin et al., 2003), especially for clayey soils. As volume change can  
57 occur when changing suction, the conventional SWRC includes the effect of this  
58 volume change. There are numerous SWRC models available in the literature, such as  
59 Brooks and Corey model (Brooks and Corey, 1964), van Genuchten model (Van  
60 Genuchten, 1980) and Fredlund and Xing model (Fredlund and Xing, 1994), to name  
61 only a few. But these models do not account for the volume change effect. Fredlund  
62 (2018) proposed mathematical algorithms combining the shrinkage curve and the  
63 SWRC, allowing for the separation of volume change effect from the effect of degree  
64 of saturation.

65

66 Based on the pore size distribution (PSD) obtained from mercury intrusion  
67 porosimetry (MIP) test, the soil water retention curve in the drying path can be  
68 obtained by applying Laplace's equation (Prapaharan et al., 1985; Delage et al., 1995;

69 Romero et al., 1999; Aung et al., 2001; Simms and Yanful, 2002, 2005; Muñoz-  
70 Castelblanco et al., 2012; Hu et al., 2013). It is worth noting that the SWRC derived by  
71 MIP result represents the SWRC under constant void ratio, which is termed as  $SWRC_{MIP}$ .  
72 Accordingly, the derived degree of saturation and suction relationship is termed as  
73  $S_{rMIP-S}$ , the derived water content and suction relationship as  $w_{MIP-S}$  and the derived  
74 void ratio and suction relationship as  $e_{MIP-S}$ .

75

76 Delage et al. (1995) analysed the PSDs and the SWRCs of various geomaterials, i.e., a  
77 siliceous and a clayey sandstone, an overconsolidated clay and a compacted silt. A  
78 good agreement was observed between  $SWRC_{MIP}$  and SWRC for sandstones, while this  
79 agreement was not observed for fine-grained soils. Muñoz-Castelblanco et al. (2012)  
80 also reported a significant difference between  $SWRC_{MIP}$  and SWRC for a loess. These  
81 differences were discussed in the literature, but no conclusive explanations were given.  
82 For example, Romero et al. (1999) thought that the differences could arise from the  
83 different effects that water and dissolved salts produce on clay fabric compared to the  
84 process in mercury intrusion. While Simms and Yanful (2002) mentioned the possible  
85 pore trapping effect; that is, mercury intrusion only gives the entrance pore radius,  
86 thus somewhat overestimating the porous volume associated with the estimated  
87 diameter.

88

89 Normally, soil microstructure is sensitive to changes in water content, especially for  
90 deformable soils. Delage et al. (1995) concluded that soil water retention properties  
91 were conditioned by the microstructure changes. Muñoz-Castelblanco et al. (2012)  
92 also showed the significant effects of changes in microstructure occurring at the level

93 of clay aggregations and the growing importance of the water adsorption in the clay  
94 fraction at high suctions. The hydraulic and mechanical responses of soil take place  
95 simultaneously when it is subjected to suction changes. That is to say, the total change  
96 in degree of saturation is induced by both changes in suction and void ratio (Simms  
97 and Yanful, 2005; Mašín, 2010; Romero et al., 2011; Sun and Sun, 2012; Hu et al., 2013;  
98 Sun et al., 2014; Della Vecchia et al., 2015; Vaunat and Casini, 2017; Fredlund, 2018).  
99 Therefore, it can be deduced that microstructural changes may be the reason for the  
100 difference between the conventional SWRC and SWRC<sub>MIP</sub>, especially for deformable  
101 soils.

102

103 Recently, the coupled hydro-mechanical response due to suction changes was  
104 accounted for by several authors (Gallipoli et al., 2003; Simms and Yanful, 2005; Sun  
105 et al., 2007; Nuth and Laloui, 2008; Mašín, 2010; Hu et al., 2013; Tsiampousi et al.,  
106 2013; Fredlund, 2018). Some of them proposed the approach based on the  
107 quantitative information derived from MIP data. Simms and Yanful (2005) developed  
108 a deformable pore-network model (DPNM) to predict the SWRC based on the  
109 evolution of measured PSDs for a compacted clayey soil under isotropic loading and/or  
110 desaturation. While in the DPNM model, pores are randomly mapped in space and  
111 idealized as a network. Hu et al. (2013) formulated a hysteretic SWRC model to  
112 account for the influence of deformation on the variation of saturation based on the  
113 changes in PSD function for deformable soils. In their model, the PSD at a deformed  
114 state can be obtained by horizontal shifting and vertical scaling of the PSD function  
115 from a reference state - initial state with void ratio  $e_0$ . The premise of the model is that  
116 the overall shapes of the various PSDs can be considered to be insignificantly different

117 from each other. This is obviously too strong hypothesis for fine-grained soils as  
118 illustrated by Sun and Cui (2018), *testifying that the changes in the aggregate porosity*  
119 *were not negligible*. Romero et al. (2011) and Della Vecchia et al. (2015) proposed a  
120 physically based conceptual framework for modelling the retention behaviour of  
121 compacted clayey soils, which considers the PSD function evolution along hydraulic  
122 and mechanical paths. *However, their framework contains a large number of*  
123 *parameters to be calibrated, limiting its application.*

124

125 In this paper, drying tests were conducted on a reconstituted silty soil. The volume,  
126 suction and PSD were determined on samples at different target water contents.  
127 *Based on the obtained results, the difference between the conventional SWRC and*  
128 *the SWRC<sub>MIP</sub> derived from PSD was analysed*. Particular attention was paid to the  
129 interrelationship between the SWRC<sub>MIP</sub> families and the conventional SWRC.  
130 Moreover, a transformation model was established between SWRC and SWRC<sub>MIP</sub>,  
131 allowing the prediction of SWRC from the SWRC<sub>MIP</sub> *families*. Through this study, the  
132 water retention mechanism associated with the volume change of soil was clearly  
133 evidenced.

134

## 135 **2. MATERIAL, TESTING PROGRAM AND CALCULATING METHOD**

### 136 *2.1 Material and testing program*

137

138 An aeolian Jossigny silt was used. The liquid limit  $w_l$  is 37%, the plastic limit  $w_p$  is 19%  
139 and the shrinkage limit  $w_s$  is 12%. In the Casagrande diagram of plasticity, the soil is

140 located close to the A-line, belonging to low plasticity clay. The clay-size fraction of  
141 Jossigny silt is 34 %.

142

143 Soil slurry, with a water content 1.5 times the liquid limit mixed with deionised water,  
144 was firstly poured into several small containers. Afterwards, the samples in the  
145 containers were air-dried to different target water contents, which were selected  
146 around  $w_l$ ,  $w_p$  and  $w_s$ . The air-drying intervals were taken short - every 30 minutes - to  
147 avoid macro-cracks in samples. After each drying operation, the container was  
148 covered for several hours for water homogenisation. By repeating these steps, dried  
149 samples at different water contents were obtained.

150

151 After reaching the respective target water content, the sample was divided into 4  
152 pieces. One for water content measurement. A second for the volume measurement  
153 based on the principle of buoyancy (Delage et al., 2007; Zeng et al., 2017). A third was  
154 freeze-dried for MIP investigation (Delage and Lefebvre, 1984; Delage et al., 1996)  
155 using an Autopore IV 9500 mercury intrusion porosimeter (Micrometrics), which  
156 operated from 3.4 kPa (363.6  $\mu\text{m}$  pore) to 227.5 MPa pressure (5.5 nm pore). The last  
157 one was used for suction measurement using a chilled-mirror dew-point  
158 psychrometer (WP4C Dewpoint PotentiaMeter). To measure low suction of soil, a test  
159 apparatus consisting of an odometer cell with 70 mm inner diameter, a porous  
160 ceramic disc with an air-entry pressure of 50 kPa and a graduated tube with 6 mm  
161 inner diameter connected to a water tank was used. More details about this apparatus  
162 can be found in Feia et al. (2014) and Sun et al. (2017). Table 1 shows the indexes of  
163 samples dried to different target states.

164

## 165 2.2 Calculating method

166

167 The mercury intrusion process is assimilated to a drying process, in which a non-  
168 wetting liquid is penetrating into a porous medium full of wetting fluid (Delage et al.,  
169 1996; Muñoz-Castelblanco et al., 2012).

170

171 The pore diameter can be deduced from the mercury pressure, as follows (Romero et  
172 al., 1999):

$$173 \quad d = -\frac{4T_m \cos \theta_m}{p} \quad (1)$$

174 where  $T_m$  is the surface tension of mercury (0.485N/m);  $d$  is the pore entrance  
175 diameter ( $\mu\text{m}$ );  $\theta_m$  is the mercury-soil contact angle (taken equal to  $130^\circ$  in this study);  
176  $p$  is the external applied intrusion pressure ( $\times 10^6 \text{ N/m}^2$ ).

177

178 The cumulative intrusion void ratio ( $e_{MIP}$ ) is computed as follows:

$$179 \quad e_{MIP} = \frac{V_m}{V_s} = \frac{V_m}{m_s} \cdot G_s \cdot \rho_w \quad (2)$$

180 where  $V_s$  is the volume of soil;  $V_m$  is the volume of intruded mercury;  $m_s$  is the mass of  
181 soil;  $G_s$  is the specific gravity;  $\rho_w$  is the water unit mass.

182

183 From the derivative of the cumulative intrusion curve, the pore size density function  
184 is obtained:

$$185 \quad f = -\frac{\delta(e_{MIP})}{\delta(\lg d)} \quad (3)$$

186 Based on the PSD obtained from MIP test, the  $SWRC_{MIP}$  can be determined  
 187 (Prapaharan et al., 1985; Romero et al., 1999; Aung et al., 2001; Simms and Yanful,  
 188 2002). The relationship between matric suction ( $u_a - u_w$ ) and mercury intrusion  
 189 pressure  $p$  can be deduced from Eq. (4):

$$190 \quad u_a - u_w = -\frac{T_w \cos \theta_w}{T_m \cos \theta_m} p \quad (4)$$

191 where  $T_w$  is the surface tension of water (0.073N/m);  $\theta_w$  is the water-soil contact angle  
 192 (taken equal to  $0^\circ$  in this study).

193

194 Romero et al. (1999) suggested that the degree of saturation  $S_r$  and water content  $w$   
 195 corresponding to the equivalent applied pressure should consider the hygroscopic  
 196 water content related to the strongly attracted adsorbed water to the mineral surface  
 197 and the equivalent residual water content corresponding to the non-intruded porosity.

198 They can be expressed as follows:

$$199 \quad S_r = (1 - S_{rm}) + \frac{w_{res}}{w_{sat}} S_{rm} \quad (5)$$

$$200 \quad w = (1 - S_{rm})(w_{sat} - w_{res}) + w_{res} \quad (6)$$

201 where  $w_{sat}$  stands for the saturated gravimetric water content;  $S_{rm}$  stands for the non-  
 202 wetting mercury degree of saturation;  $w_{res}$  is the equivalent residual water content  
 203 corresponding to the maximum mercury intrusion pressure that the mercury  
 204 porosimeter can reach.

205

206  $S_{rm}$  and  $w_{res}$  can be calculated as follows:

207 
$$S_{rm} = \frac{V_m}{V_{mmax}} = \frac{e_{MIP}}{e_{MIPmax}} \quad (7)$$

208 
$$w_{res} = \frac{m_{wres}}{m_s} = \frac{\rho_w (V_v - V_{mmax})}{m_s} = \frac{e - e_{MIPmax}}{G_s} \quad (8)$$

209

210 Finally,

211 
$$w_{MIP} = \frac{e}{G_s} \left(1 - \frac{e_{MIP}}{e}\right) \quad (9)$$

212 
$$S_{rMIP} = 1 - \frac{e_{MIP}}{e} \quad (10)$$

213 where  $e_{MIP}$  is the mercury intruded void ratio;  $e_{MIPmax}$  is the maximum mercury  
 214 intruded void ratio;  $e$  is the void ratio corresponding to different target drying states;  
 215  $S_{rMIP}$  is the degree of saturation obtained from MIP test;  $w_{MIP}$  is the water content  
 216 derived from MIP test.

217

218 Based on the above measurements and calculations, the void ratios and degrees of  
 219 saturation of soil samples at different target water contents were calculated, and the  
 220 conventional SWRC and the SWRC<sub>MIP</sub> derived from PSD were also determined.

221

## 222 3 EXPERIMENTAL RESULTS

223

### 224 3.1 Shrinkage behaviour and conventional SWRC

225

226 Figure 1 shows the results from the drying tests on the reconstituted Jossigny silt  
 227 prepared at initial water content  $w_i = 1.5 w_l$ . Figs. 1 (a) and (c) depict the shrinkage

228 behaviour, e.g., the changes of void ratio with water content ( $e - w$ ), and degree of  
229 saturation with water content ( $S_r - w$ ), respectively. Fig. 1(b) depicts the volume  
230 change behaviour under the effect of suction, e.g., void ratio with suction ( $e-s$ ). Figs.  
231 1(d) shows the conventional  $S_r$ -SWRC of Jossigny silt.

232

233 The  $e-w$  relationship obeys a typical shrinkage characteristic curve of soils, as shown  
234 in Fig. 1(a), which includes normal shrinkage, residual shrinkage and no shrinkage  
235 stages. The experimental results firstly started from the stage of normal shrinkage,  
236 which coincided with the dashed full saturation line, and the samples kept fully  
237 saturated, as shown in Fig. 1(c) for the  $S_r-w$  relationship. Afterwards, when water  
238 content reached  $w_{ae}$ , the slope of the shrinkage curve decreased, and the residual  
239 shrinkage began. From the air entry point, the degree of saturation began to decline,  
240 as it can be seen from the  $S_r-w$  curve in Fig. 1(c). From the  $S_r$ -SWRC in Fig. 1(d), the  
241 corresponding suction at  $w_{ae}$  could be determined of about 180 kPa. When suction  $s$   
242 exceeded the air entry value,  $S_r$ -SWRC changed from the saturated to the unsaturated  
243 domain. After the water content reached the shrinkage limit  $w_s$ , the void ratio  
244 remained unchanged with further drying, as shown in Fig. 1(a) and (b), starting the no  
245 shrinkage stage.

246

### 247 *3.2 Microstructure investigation*

248 Figure 2 presents the pore size distribution of Jossigny silt during drying. Fig. 2(a) is the  
249 cumulative intruded curves. It can be observed that  $e_{MIP}$  decreased in the beginning  
250 and became almost unchanged after the water content reached the shrinkage limit.

251 The pore size density functions shown in Fig. 2(b) are the derivative of the cumulative

252 intrusion curves of No. (1)-(6) in Fig. 2(a), plotted in terms of  $\delta e_{MIP}/\delta \lg d$  as a function  
253 of pore entrance diameter  $d$ . From Fig. 2(b), all the PSD curves present a typical  
254 unimodal pattern (Fiès and Bruand, 1998). When  $w > w_s$ , significant pore refinement  
255 occurred upon drying. However, with further drying, the curves began shifting to  
256 larger diameter. Sun and Cui (2018) explained this phenomenon by the development  
257 of possible micro-fissures of the clay part. Moreover, when  $w < w_s$ , the shift trend of  
258 PSD curves ceased. Accordingly, the void ratio at this time almost remained  
259 unchanged and reached the minimum value,  $e_{min}$ .

260

### 261 3.3 SWRC<sub>MIP</sub> derived from MIP investigations

262

263 Figure 3 presents the relationship between degree of saturation and suction. The plots  
264 star (★) show the conventional SWRC results determined directly by suction  
265 measurement, the others corresponding to the samples with different target water  
266 contents. It can be noticed that the SWRC<sub>MIP</sub> significantly differs from the conventional  
267 SWRC.

268

269 SWRC<sub>MIP</sub> can be divided into three segments on a semi-logarithmic plot, that is, a  
270 boundary effect zone, a transition zone and a residual zone:

271

272 (i) In the boundary effect zone,  $S_{rMIP}$  was almost equal to 100%, where almost no  
273 mercury intrusion took place.

274

275 (ii) In the transition zone, sudden drops occurred because of the intrusion of the  
276 dominant pore diameters. It was also observed that the  $S_{rMIP-s}$  curve shifted towards  
277 the  $S_r-s$  curve at the beginning, however in the residual shrinkage stage, the  $S_{rMIP-s}$   
278 curve began to shift backwards due to the possible presence of drying-induced  
279 internal micro-fissures occurred in the clay fractions and in the interface between silt  
280 grain and clay particles, more details can be found in Sun and Cui (2018).

281

282 (iii) In the residual zone, the  $S_{rMIP-s}$  curves showed a shifting-up with further drying,  
283 and got close to the  $S_r-s$  curve. The  $S_{rMIP}$  represents the volume fraction of the non-  
284 intruded space and can be expressed as  $S_{rMIP}=(e-e_{MIP})/e$  in Eq.(10). The shifting-up of  
285 the  $S_{rMIP-s}$  curve in the residual zone was the result of the changes of non-intruded  
286 void ratio ( $e-e_{MIP}$ ). The changes of  $S_{rMIP-s}$  curves were also related to the  
287 microstructure change during drying. Moreover, it could be deduced according to the  
288 shifting-up trend that the  $S_{rMIP-s}$  curve of sample with the smallest void ratio ( $e=e_{min}$ )  
289 almost reached the  $S_r-s$  curve. At this time, the  $SWRC_{MIP}$  from MIP test is the same as  
290 the conventional SWRC, in agreement with the observation of Delage et al. (1995).

291

### 292 3.4 $S_r-s$ & $S_{rMIP-s}$ relationships

293

294 Figure 4 shows the sketch of  $S_r-s$  relationship (solid line from A to B) and  $S_{rMIP-s}$   
295 relationship (dash line from A to C). Point A marks the coordinate ( $S_{ri}, s_i$ ) with void ratio  
296  $e_i$  and water content  $w_i$ , and Point B ( $S_{ri+1}, s_{i+1}$ ) with void ratio  $e_{i+1}$  and water content  
297  $w_{i+1}$ . From A to B, when the suction increased from  $s_i$  to  $s_{i+1}$ , the degree of saturation

298 decreased from  $S_{ri}$  to  $S_{ri+1}$ . The absolute change value in degree of saturation when  
299 suction increased from  $s_i$  to  $s_{i+1}$  is  $|dS_r| = |S_{ri+1} - S_{ri}|$ .

300

301 The change in degree of saturation at constant void ratio  $e_i$  when suction increased  
302 from  $s_i$  to  $s_{i+1}$  followed the  $S_{rMIP-s}$  curve from A to C, and could be described as  $|dS_r(s)$   
303  $e = e_i|$ , which could be obtained by the  $S_{rMIP-s}$  curve at constant void ratio  $e_i$ , i.e.,  $dS_r(s)$   
304  $e = e_i = dS_{rMIP e = e_i}$ .

305

306 Therefore, the change in degree of saturation caused by void ratio change under a  
307 constant suction ( $s = s_i$ ) could be determined as  $|dS_r(e)_{s = s_i}|$ , and it could be calculated  
308 by  $|dS_r(e)_{s = s_i}| = |dS_r(s)_{e = e_i}| - |dS_r|$ .

309

310 From the drying tests, the relationships between degree of saturation and suction ( $S_r$ -  
311  $s$ ) and between void ratio and suction ( $e$ - $s$ ) were obtained. Combined with the MIP  
312 results, the changes of  $|dS_r(e)| / |dS_r(s)|$  and  $|dS_r| / |dS_r(s)|$  with suction were  
313 determined, as shown in Fig. 5. It can be seen from the changes in  $|dS_r(e)| / |dS_r(s)|$   
314 (dash line) that with increasing suction, the value changes from 1 to 0 gradually,  
315 indicating that when suction is low, the reduction of degree of saturation is mainly  
316 caused by the changes of void ratio. By contrast, when the water content reached the  
317 shrinkage limit, the void ratio kept almost unchanged, and the contribution of void  
318 ratio to the change of degree of saturation  $|dS_r|$  vanished. Conversely, with  
319 increasing suction, the value  $|dS_r| / |dS_r(s)|$  changed from 0 to 1 gradually, indicating  
320 that when suction was low, the degree of saturation almost kept 100%. At higher

321 suction, the void ratio tended to become unchanged and the change of degree of  
322 saturation was totally caused by suction change, that is,  $|dS_r| = |dS_r(s)|$ .

323

324 For non-deformable soils, the  $S_{rMIP-s}$  curves are consistent with the  $S_r-s$  curve (Delage  
325 et al., 1995), the value  $|dS_r| / |dS_r(s)|$  can be approximately taken equal to 1. On  
326 the contrary, for deformable soils, the shapes of  $S_{rMIP-s}$  curve and  $S_r-s$  curve differ  
327 significantly and the value  $|dS_r| / |dS_r(s)|$  changes from 0 to 1 gradually with the  
328 increase of suction.

329

### 330 *3.5 $S_r-e-s$ & $S_{rMIP-e-s}$ three-dimension surfaces*

331

332 In order to better visualise the effect of void ratio on SWRC, two diagrams are  
333 proposed: one is the  $S_r-e-s$  three-dimension diagram and another is the  $S_{rMIP-e-s}$  three-  
334 dimension diagram, as shown in Fig. 6. The conventional SWRC is located on the  $S_r-e-$   
335  $s$  3D surface with void ratio changing, while the  $SWRC_{MIP}$  with constant void ratio is  
336 located on the  $S_{rMIP-e-s}$  3D surface.

337

338 The F-X equation (Fredlund and Xing, 1994), with the applied correction factor for zero  
339 water content at  $10^6$  kPa of suction, was adopted in building the three-dimension  
340 surface for further investigation, as shown in equation (11). However, it is worth  
341 noting that other suitable models can be also used provided that they allow the  
342 description of the data over the full suction range.

$$343 \quad S_r = \left( 1 - \frac{\ln(1 + s / s_{res})}{\ln(1 + 10^6 / s_{res})} \right) \left[ \frac{1}{\ln(2.718 + (s / a)^n)} \right]^m \quad (11)$$

344 where  $s$  is suction;  $s_{res}$  is the suction corresponding to the equivalent residual water  
345 content; parameters  $a$ ,  $n$ , and  $m$  affect the shape of the curve.

346

347 The  $S_{rMIP}-e-s$  three-dimension surface can be obtained by the following method: first,  
348 the  $S_{rMIP}-s$  curve at constant void ratio  $e = e_i$  was derived from the PSD curve obtained  
349 from MIP test. Second, each  $S_{rMIP}-s$  ( $e = e_i$ ) relationship was expressed through the F-  
350 X SWRC model, namely formula (11), each curve having its corresponding three  
351 parameters  $a(e_i)$ ,  $n(e_i)$ ,  $m(e_i)$ . Thus, the function of the parameter changing with the  
352 void ratio could be determined. Finally, the  $S_{rMIP}-e-s$  three-dimension surface was built.

353

354 From the  $w-s$  relationship matched by the F-X SWRC model and the equation  $e S_r = G_s$   
355  $w$ , the  $S_r-e-s$  surface was obtained. After that, several SWRCs at constant void ratio  
356 were obtained through the F-X SWRC model.

357

358 Figure 7 shows the projection of drying test results in  $S_r(S_{rMIP})-e-s$  diagram, the thick  
359 solid curve is the conventional SWRC in drying path obtained in this study, and the  
360 thick dash curve is the SWRC projection on the  $S_{rMIP}-e-s$  surface. The projections of the  
361 two thick curves onto  $S_r(S_{rMIP})-o-s$ ,  $S_r(S_{rMIP})-o-e$ , and  $e-o-s$  surfaces are also shown. It  
362 is worth noting that, in  $S_r-o-s$  coordinate, the projection of the thick solid curve is  
363 conventional  $S_r-s$  relationship in drying path, with void ratio changing following the  
364 projection in  $e-o-s$  coordinate.

365

366 The projection of drying test results on  $e-o-s$  coordinate is shown in Fig.1(b). It can be  
367 observed that the void ratio decreased with increasing suction. Figure 8 shows the

368 sketch of  $e$ - $s$  relationship corresponding to the drying test result. It can be seen that  
369 each suction  $s_i$  had a corresponding relationship with the void ratio  $e_i$ . Combing the  
370 test results in Fig.1(b) and the sketch of  $e$ - $s$  relationship in Fig.8, it is observed that the  
371 water content reached the shrinkage limit at  $w_s=12\%$ , corresponding to suction  $s_s$   
372  $=1500$  kPa and void ratio is  $e_s=0.52$ . Under further drying, the void ratio remained  
373 almost unchanged. When suction reached  $10^6$  kPa, the void ratio reached the  
374 minimum value:  $e=e_{\min}$  (about 0.49).

375

376 Figure 9 shows the projection of the test results on  $S_r$  ( $S_{rMIP}$ )- $o$ - $s$  coordinate. The plots  
377 star ( $\star$ ) show the conventional SWRC results obtained in this study. Correspondingly,  
378 the thick solid curve represents the conventional  $S_r$ - $s$  relationship. The dash dot curve  
379 represents the  $S_{rMIP}$ - $s$  ( $e=e_i$ ) curve, which can be regarded as one of the MIP test results  
380 in the study, or as one of the curves selected from the  $S_{rMIP}$ - $e$ - $s$  surface at any void  
381 ratio  $e_i$ . It is to be mentioned that the corresponding  $S_{rMIP}$ - $s$  ( $e=e_{\min}$ ) curve, represented  
382 by a dash curve, was obtained from the established  $S_{rMIP}$ - $e$ - $s$  three-dimension surface  
383 at  $e=e_{\min}$ .

384

385 As observed previously, the  $S_{rMIP}$ - $s$  curve moved rightwards with void ratio decreasing  
386 under the premise that there are no micro-fissures developed during drying. After the  
387 water content reached the shrinkage limit, the void ratio approached the minimum  
388 value  $e_{\min}$  gradually. It can be reasonably assumed that the  $S_r$ - $s$  ( $e=e_{\min}$ ) curve in  $S_r$ - $e$ - $s$   
389 3D surface, the  $S_{rMIP}$ - $s$  ( $e=e_{\min}$ ) relationship in  $S_{rMIP}$ - $e$ - $s$  3D surface and the projection  
390 of the conventional  $S_r$ -SWRC on  $S_r$ - $o$ - $s$  coordinate coincide in the high suction range.  
391 This is testified in Fig. 9. Therefore, the  $S_{rMIP}$ - $s$  ( $e=e_{\min}$ ) curve can be taken as the

392 reference curve, which connects the two surfaces,  $S_{rMIP-e-s}$  and  $S_r-e-s$ .

393

#### 394 4. TRANSFORMATION FROM $S_{rMIP-s}$ CURVES TO CONVENTIONAL $S_r-s$ RELATIONSHIP

395

396 From above analysis, it is noticed that a  $SWRC_{MIP}$  corresponds to a fixed pore structure,

397 however, a real SWRC is affected by soil volume changes. It can also be deduced that

398  $S_{rMIP-s}$  curves would move continuously toward the  $S_r-s$  curve under the condition of

399 no micro-fissures occurring, i.e., theoretically, a SWRC is the combination of a family

400 of  $SWRC_{MIPs}$  at different suctions. Based on the finding that the  $S_{rMIP-s}$  ( $e=e_{min}$ ) curve

401 can be taken as a reference curve, connecting the  $S_{rMIP-e-s}$  and the  $S_r-e-s$  surfaces, a

402 transformation model was established to predict the SWRC from the  $SWRC_{MIP}$  families,

403 accounting for the effect of soil volume change on soil water retention property.

404

##### 405 4.1 Transformation model

406

407 As the conventional  $S_r-SWRC$  coincides with the  $S_{rMIP-s}$  curve at  $e=e_{min}$ , as shown in Fig.

408 9, namely  $S_r(s=s_i, e=e_i) = S_{rMIP}(s=s_i, e=e_{min})$ , the difference between  $S_r$  on the  $S_r-e-s$

409 surface and  $S_{rMIP}$  on the  $S_{rMIP-e-s}$  surface when  $s=s_i$ , combined with Eq.(10), can be

410 expressed as:

$$411 \quad S_r(s=s_i, e=e_i) - S_{rMIP}(s=s_i, e=e_i) \quad (13)$$

$$412 \quad = S_{rMIP}(s=s_i, e=e_{min}) - S_{rMIP}(s=s_i, e=e_i)$$

$$413 \quad = 1 - \frac{e_{MIP}(s=s_i, e=e_{min})}{e_{min}} - 1 + \frac{e_{MIP}(s=s_i, e=e_i)}{e_i}$$

414 
$$= \frac{e_{MIP}(s=s_i, e=e_i)}{e_i} - \frac{e_{MIP}(s=s_i, e=e_{min})}{e_{min}}$$

415 where  $e_{MIP}(s=s_i, e=e_i)$  represents the amount of mercury intrusion for soil sample with  
 416 void ratio equals  $e_i$ , and with pore diameter  $d \geq d_i$  and corresponding  $s \leq s_i$ . Figure 10  
 417 shows the  $e_{MIP}$ - $s$  relationship, the solid curve represents the condition of  $e=e_i$ ,  $e_{MIP}(s=s_i,$   
 418  $e=e_i)$  is namely the mercury intrusion porosity ratio when  $e=e_i$ ,  $s \leq s_i$  and  $d \geq d_i$ , and the  
 419 dash curve represents the condition of  $e=e_{min}$ ,  $e_{MIP}(s=s_i, e=e_{min})$  is namely the mercury  
 420 intrusion porosity ratio when  $e=e_{min}$ ,  $s \leq s_i$  and  $d \geq d_i$ .

421

422 Figure 11 shows the pore size distribution diagram, which shows the change of PSD  
 423 function when  $e$  decreases from  $e_i$  to  $e_{min}$ .  $e_{MIP}(s=s_i, e=e_i)$  and  $e_{MIP}(s=s_i, e=e_{min})$  can be  
 424 expressed as:

425 
$$\begin{aligned} e_{MIP}(s=s_i, e=e_i) &= A_{d \geq d_i}(e=e_i) \cdot e_i \\ e_{MIP}(s=s_i, e=e_{min}) &= A_{d \geq d_i}(e=e_{min}) \cdot e_{min} \end{aligned} \quad (14)$$

426 where  $A_{d \geq d_i}(e=e_i)$  represents the porosity proportion of  $d \geq d_i$ , which is the proportion  
 427 of the shaded area with cross grain on the PSD curve of  $e=e_i$ , and  $A_{d \geq d_i}(e=e_{min})$   
 428 represents the porosity proportion of  $d \geq d_i$ , which is the proportion of the shaded  
 429 area with vertical stripe on the PSD curve of  $e=e_{min}$ . When the void ratio decreases to  
 430  $e_{i+n}$ , the pore entrance diameter decreases to  $d_{i+n}$ , and the corresponding suction  
 431 increases to  $s_{i+n}$ , and  $e_{MIP}(s=s_{i+n}, e=e_{i+n})$  and  $e_{MIP}(s=s_{i+n}, e=e_{min})$  can be obtained by the  
 432 above method, combined with Fig.11.

433

434 Therefore, the difference  $(S_r - S_{rMIP})$  at  $s=s_i$ , in Eq.(13), can be further expressed as:

435 
$$S_r (s = s_i, e = e_i) - S_{rMIP} (s = s_i, e = e_i) = A_{d \geq d_i} (e = e_i) - A_{d \geq d_i} (e = e_{min}) \quad (15)$$

436 It appears from Fig. 6 that the variation between  $S_r$  and  $S_{rMIP}$ , i.e.,  $(S_r - S_{rMIP})$  at  $s=s_i$ ,  
 437 which is simplified as  $Y_i$ , represents the distance between Point A on  $S_r$ - $e$ - $s$  3D surface  
 438 and Point  $A_M$  on  $S_{rMIP}$ - $e$ - $s$  3D surface. When  $s=s_{i+1}$ , the variation between  $S_r$  and  $S_{rMIP}$  at  
 439  $s= s_{i+1}$ , simplified as  $Y_{i+1}$ , represents the distance between Point B on  $S_r$ - $e$ - $s$  3D surface  
 440 and Point  $B_M$  on  $S_{rMIP}$ - $e$ - $s$  3D surface.

441

442 The variation between  $Y_{i+1}$  and  $Y_i$ , e.g.,  $\Delta Y$  represents the change of the value  $(S_r -$   
 443  $S_{rMIP})$  from point  $s=s_i$  to point  $s=s_{i+1}$ . It can be expressed as:

444 
$$\Delta Y = Y_{i+1} - Y_i \quad (16)$$

445 
$$= (S_r - S_{rMIP})_{(s=s_{i+1}, e=e_{i+1})} - (S_r - S_{rMIP})_{(s=s_i, e=e_i)}$$

446 
$$= (A_{s \leq s_{i+1}} (e = e_{i+1}) - A_{s \leq s_{i+1}} (e = e_{min})) - (A_{s \leq s_i} (e = e_i) - A_{s \leq s_i} (e = e_{min}))$$

447 To summarize, according to Eq.(16),  $\Delta Y$  can be obtained by the following steps:

448

449 First, the  $S_{rMIP}$ - $e$ - $s$  surface can be obtained from at least three MIP experiment results  
 450 of samples with different void ratios. Second, the  $S_{rMIP}$ - $s$  relationship for any void ratio  
 451  $e_i$  and the minimum void ratio  $e_{min}$  can be obtained from the deduced  $S_{rMIP}$ - $e$ - $s$  surface.

452 Then, the relationships of  $e_{MIP}$ - $s$  at  $e=e_i$  and  $e=e_{min}$  can be back deduced by the

453 obtained  $S_{rMIP}$ - $s$  relationship. The proportional "A" value in Eq.(16) can be obtained

454 from the  $e_{MIP}$ - $s$  curves of  $e=e_i$  and  $e=e_{min}$  or their pore size distribution curves. Finally,

455 the variation  $Y_i$  between  $S_r$  and  $S_{rMIP}$  at  $s=s_i$  in Eq.(15) can be obtained. Given the

456 suction increasing step, and the suction reaches  $s=s_{i+1}$ , by repeating the above

457 procedures,  $Y_{i+1}$  between  $S_r$  and  $S_{rMIP}$  at  $s= s_{i+1}$  can also be obtained.

458

459 Simultaneously, from Fig. 6,  $\Delta Y$  can also be expressed **geometrically** as:

460 
$$\Delta Y = (S_{r_{i+1}} - S_{r_{MIP_{i+1}}}) - (S_{r_i} - S_{r_{MIP_i}}) = S_{r_{i+1}} - S_{r_i} - (S_{r_{MIP_{i+1}}} - S_{r_{MIP_i}}) \quad (17)$$

461 where  $S_{r_{MIP_{i+1}}} - S_{r_{MIP_i}} = \Delta S_{r_{MIP(i+1)-(i)}}$  corresponds to the variation of degree of saturation

462 on the  $S_{r_{MIP}}-e-s$  three-dimension surface, and includes two parts: one caused by

463 changes of suction and the other caused by changes of void ratio, which can be

464 expressed by the following integral:

465 
$$dS_{r_{MIP}}(s_i \rightarrow s_{i+1}, e_i \rightarrow e_{i+1}) = \frac{\partial S_{r_{MIP}}}{\partial e} de + \frac{\partial S_{r_{MIP}}}{\partial s} ds \quad (18)$$

466

467 Finally, using the values of the degree of saturation and water content at suction  $s_i$ ,

468 combining Eqs. (16)-(18), the  $S_{r_{i+1}}$  and  $w_{i+1}$  at  $s_{i+1}$  can be deduced, as follows:

469 
$$S_{r_{i+1}} = Y_{i+1} - Y_i + S_{r_i} + \Delta S_{r_{MIP(i+1)-(i)}} \quad (19)$$

470 
$$w_{i+1} = \frac{e_{i+1} \cdot S_{r_{i+1}}}{G_s} \quad (20)$$

471 Subsequently, the conventional SWRC is predicted from the  $SWRC_{MIP}$  families

472 according to the transformation model.

473

474 In summary, in the transformation model, the  $S_r-e-s$  three-dimension surface where

475 conventional SWRC is located and  $S_{r_{MIP}}-e-s$  three-dimension surface where the

476  $SWRC_{MIP}$  with void ratio unchanging is located were defined. Based on the finding that

477 the  $S_r-s$  ( $e=e_{min}$ ) curve, the  $S_{r_{MIP}}-s$  ( $e=e_{min}$ ) relationship and the conventional  $S_r$ -SWRC

478 coincide at high suction, the soil state with no longer volume change is taken as a

479 reference, that is,  $S_{r_{MIP}}-s$  ( $e=e_{min}$ ) curve, which connects the two surfaces,  $S_{r_{MIP}}-e-s$  and

480  $S_r$ - $e$ - $s$ . After that, based on the evolution of PSD curves due to the porosity changes,  
481 and the variation of  $S_{rMIP}$  deduced from the  $S_{rMIP}$ - $e$ - $s$  three-dimension surface, the  
482 degree of saturation can be determined. Finally, the conventional  $S_r$ -SWRC is obtained.  
483 It is worth noting that the transformation model introduces no more parameters than  
484 those in the F-X model.

485

486 The transformation model is suitable for saturated samples undergoing drying test, no  
487 matter what stress histories they have before saturation. Upon wetting, the  $S_{rMIP}$ - $s$   
488 curve would shift leftwards due to soil swelling (increase of porosity). Theoretically,  
489 the same philosophy of analysis can be applied. This is to be verified later when  
490 experimental data are available.

491

#### 492 *4.2 Application of the transformation model*

493

494 Applying the proposed approach, the transformation was completed from the  
495  $SWRC_{MIP}$  families to the conventional SWRC. Fig. 12 shows the comparison between  
496 the experimental and predicted SWRC from the  $SWRC_{MIP}$  families of reconstituted  
497 Jossigny silt in drying, including  $S_r$ - $s$  relationship in Fig. 12(a) and  $w$ - $s$  relationship in  
498 Fig. 12(b).

499

500 According to the shrinkage curve of reconstituted Jossigny silt, the minimum void ratio  
501  $e_{min}$  is 0.49. In Fig. 12(a), the marks of “★” shows the SWRC test results; the solid curve  
502 represents the predicted  $S_r$ - $s$  relationship curve by the transformation model; the  
503 marks “□” represents the  $S_{rMIP}$ - $s$  relationship, which is obtained as follows: given the

504 suction increasing step, the corresponding void ratio is obtained by the  $e$ - $s$  curve, and  
505 each point in  $e$ - $s$  curve corresponds to a point on the obtained  $S_{rMIP}$ - $e$ - $s$  surface. Then,  
506 these points are projected on the  $S_r$  ( $S_{rMIP}$ )- $o$ - $s$  coordinate, and the  $S_{rMIP}$ - $s$  relationship  
507 can be obtained.

508

509 It can be seen that the  $S_r$ - $s$  and the  $w$ - $s$  relationship curves predicted by the  
510 transformation model are in good agreement with the measured SWRC results,  
511 testifying the validity of the proposed model and indicating that the proposed model  
512 can satisfactorily account for the influence of soil volume change on its water  
513 retention property.

514

## 515 **5 CONCLUSIONS**

516

517 In order to analysis the difference between the conventional SWRC and  $SWRC_{MIP}$   
518 derived from PSD due to volume change, drying test was conducted on a reconstituted  
519 silty soil, together with the volume, suction and PSD measurements. The changes of  
520 the  $SWRC_{MIP}$  families and their relation with conventional SWRC were analyzed. It can  
521 be concluded that deformation of the soil is the main reason for the difference  
522 between the conventional SWRC and  $SWRC_{MIP}$ .

523

524 A transformation model was proposed further. The model is based on the finding that  
525 the  $S_r$ - $s$  ( $e=e_{min}$ ) curve in  $S_r$ - $e$ - $s$  3D surface, the  $S_{rMIP}$ - $s$  ( $e=e_{min}$ ) relationship in the  $S_{rMIP}$ -  
526  $e$ - $s$  3D surface and the projection of the conventional SWRC on  $S_r$  ( $S_{rMIP}$ )- $o$ - $s$  coordinate  
527 coincide at high suctions. This model takes the soil state with no longer volume change

528 as a reference, and takes the  $S_{rMIP-s}$  ( $e=e_{min}$ ) curve as a reference curve in  $S_r$ -SWRC  
529 prediction, which connects the  $S_{rMIP-e-s}$  and  $S_r-e-s$  surfaces. The model is expected to  
530 be suitable for undisturbed and compacted-saturated samples undergoing drying  
531 path, no matter what stress histories they have before saturation.

532

### 533 **ACKNOWLEDGEMENTS**

534

535 The authors are grateful to the China Scholarship Council (CSC Grand No.  
536 201406895026), Ecole des Ponts ParisTech, Shanghai Key Innovative Team of Cultural  
537 Heritage Conservation, the National Sciences Foundation of China (Grant No.  
538 41572284, 41977214) and the Open Research Fund of State Key Laboratory of  
539 Geomechanics and Geotechnical Engineering, Institute of Rock and Soil Mechanics,  
540 Chinese Academy of Sciences (Grant No. Z013008) for the financial supports.

541

### 542 **References**

543 Aubertin M, Mbonimpa M, Bussière, B, et al. A model to predict the water retention curve from  
544 basic geotechnical properties. Canadian Geotechnical Journal, 2003; 40(6):1104-1122.

545 Aung K K, Rahardjo H, Leong E C, et al. Relationship between porosimetry measurement and soil-  
546 Water characteristic curve for an unsaturated residual soil. Geotechnical and Geological  
547 Engineering, 2001; 19(3):401-416.

548 Brooks RH, Corey AT. Hydraulic properties of porous media, *Colorado State University, Fort Collins, CO*,  
549 1964; Hydrology Paper, (3): 27.

550 Delage P, Lefebvre G. Study of the structure of a sensitive Champlain clay and of its evolution  
551 during consolidation. Canadian Geotechnical Journal, 1984; 21(1):21-35.

552 Delage P, Audiguier M, Cui Y J, et al. Propriétés de rétention d'eau et microstructure de différents

553 géomatériaux. XIème Conférence Européenne de Mécanique des Sols et des Travaux de  
554 Fondations. 1995; 3:43-48.

555 Delage P, Audiguier M, Cui Y J, et al. Microstructure of a compacted silt. Canadian Geotechnical  
556 Journal, 1996; 33(1):150-158.

557 Delage P, Le T T, Tang A M, et al. Suction effects in deep Boom Clay block samples. Géotechnique,  
558 2007; 57(2):239-244.

559 Della Vecchia G, Dieudonné Anne-Catherine, Jommi C, et al. Accounting for evolving pore size  
560 distribution in water retention models for compacted clays. International Journal for  
561 Numerical and Analytical Methods in Geomechanics, 2015; 39(7):702-723.

562 Feia S, Ghabezloo S, Bruchon J F, et al. Experimental evaluation of the pore-access size distribution  
563 of sands. Geotechnical Testing Journal, 2014; 37(4): 613-620.

564 Fiès J C, Bruand A. Particle packing and organization of the textural porosity in clay–silt–sand  
565 mixtures. European Journal of Soil Science, 1998; 49(4): 557-567.

566 Fredlund D G, Xing A. Equations for the soil-water characteristic curve. Canadian Geotechnical  
567 Journal, 1994; 31(4):521-532.

568 Fredlund D G. Role of the soil-water characteristic curve in unsaturated soil mechanics. The 7<sup>th</sup>  
569 International Conference on Unsaturated Soils UNSAT 2018. Editors: Charles W. W. Ng,  
570 Anthony K. Leung, Abraham C.F. Chiu & Chao Zhou. Blight Lecture. Hong Kong, 2018.

571 Gallipoli D, Wheeler S J, Karstunen M. Modelling the variation of degree of saturation in a  
572 deformable unsaturated soil. Géotechnique, 2003; 53(1):105-112.

573 Hu R, Chen Y F, Liu H H, et al. A water retention curve and unsaturated hydraulic conductivity  
574 model for deformable soils: Consideration of the change in pore-size distribution.  
575 Géotechnique, 2013; 63(16): 1389-1405.

576 Mašín D. Predicting the dependency of a degree of saturation on void ratio and suction using  
577 effective stress principle for unsaturated soils. International Journal for Numerical and  
578 Analytical Methods in Geomechanics, 2010; 34(1): 73-90.

579 Munoz-Castelblanco J A, Pereira J M, Delage P, et al. The water retention properties of a natural  
580 unsaturated loess from northern France. *Géotechnique*, 2012; 62(2): 95-106.

581 Nuth M, Laloui L. Advances in modelling hysteretic water retention curve in deformable soils.  
582 *Computers and Geotechnics*, 2008; 35(6):835-844.

583 Prapaharan S, Altschaeffl A G, Dempsey B J. Moisture Curve of Compacted Clay: Mercury Intrusion  
584 Method. *Journal of Geotechnical Engineering*, 1985; 111(9):1139-1143.

585 Romero E, Gens A, Lloret A. Water permeability, water retention and microstructure of unsaturated  
586 compacted Boom clay. *Engineering Geology*, 1999; 54(1-2):117-127.

587 Romero E, Della Vecchia G, Jommi C. An insight into the water retention properties of compacted  
588 clayey soils. *Géotechnique*, 2011; 61(4): 313-328.

589 Simms P H, Yanful E K. Predicting soil-water characteristic curves of compacted plastic soils from  
590 measured pore-size distributions. *Géotechnique*, 2002; 52(4):269-278.

591 Simms P H, Yanful E K. A pore-network model for hydromechanical coupling in unsaturated  
592 compacted clayey soils. *Canadian Geotechnical Journal*, 2005; 42(2):499-514.

593 Sun D A, Sheng D C, Sloan S W. Elastoplastic modelling of hydraulic and stress-strain behaviour of  
594 unsaturated soils. *Mechanics of Materials*, 2007; 39(3):212-221.

595 Sun W J, Cui Y J. Investigating the microstructure changes for silty soil during drying. *Géotechnique*,  
596 2018; 68(4): 370-373.

597 Sun W J, Sun D A. Coupled modelling of hydro-mechanical behaviour of unsaturated compacted  
598 expansive soils. *International Journal for Numerical and Analytical Methods in Geomechanics*,  
599 2012; 36(8):1002-1022.

600 Sun W J, Sun D A, Fang L, et al. Soil-water characteristics of Gaomiaozi bentonite by vapour  
601 equilibrium technique. *Journal of Rock Mechanics and Geotechnical Engineering*, 2014;  
602 6(1):48-54.

603 Sun W J, Cui Y J, Hong Z S, et al. Moisture tension in fine-grained reconstituted soils at high initial  
604 water contents. *UNSAT-WASTE 2017, Shanghai, 2017: 131-138.*

605 Tsiampousi A, Zdravkovic L, Potts D M. A three-dimensional hysteretic soil-water retention curve.  
606 *Géotechnique*, 2013; 63(2): 155-164.

607 van Genuchten MT. A closed-form equation for predicting the hydraulic conductivity of unsaturated  
608 soils. *Journal of Soil Science Society of America*, 1980; 44: 892-898.

609 Vaunat J, Casini F. A procedure for the direct determination of Bishop's  $\chi$  parameter from changes  
610 in pore size distribution. *Géotechnique*, 2017; 67(7): 631-636.

611 Wheeler S J. Inclusion of specific water volume within an elasto-plastic model for unsaturated soil.  
612 *Canadian Geotechnical Journal*, 1996; 33(1): 42-57.

613 Zeng L L, Cui Y J, Conil N, et al. Experimental study on swelling behaviour and microstructure  
614 changes of natural stiff Teguline clays upon wetting. *Canadian Geotechnical Journal*, 2017;  
615 54(5): 700-709.

616

617 **List of Tables**

618 Table 1. Indexes of samples drying to different target states

619

620 **List of Figures**

621 Fig. 1 Results of the drying process of reconstituted Jossigny silt with  $w_i = 1.5 w_L$

622 Fig. 2 Pore size distribution of Jossigny silt during drying (data after Sun and Cui, 2018)

623 Fig. 3  $S_{rMIP}$ - $s$  relationships and  $S_r$ - $s$  relationship

624 Fig. 4  $S_r$  ( $S_{rMIP}$ ) -  $s$  relationship

625 Fig. 5 Changes of  $dS_r(e)/dS_r(s)$  &  $dS_r/dS_r(s)$  with suction

626 Fig. 6  $S_r$  ( $S_{rMIP}$ )- $e$ - $s$  three-dimension diagram

627 Fig. 7 Projection of drying test results in  $S_r$  ( $S_{rMIP}$ )- $e$ - $s$  three-dimension diagram

628 Fig. 8  $e$ - $s$  relationship

629 Fig. 9 Comparison and connection between  $S_{rMIP}$ - $s$  and  $S_r$ - $s$  relationship

630 Fig. 10  $e_{MIP}$ - $s$  relationship

631 Fig. 11 Change of PSD function with void ratio decreasing from  $e=e_i$  to  $e_{min}$

632 Fig. 12 Transformation of  $SWRC_{MIP}$  to conventional SWRC in drying of reconstituted

633 Jossigny silt

634

635 List of Tables

636 Table 1. Indexes of samples drying to different target states

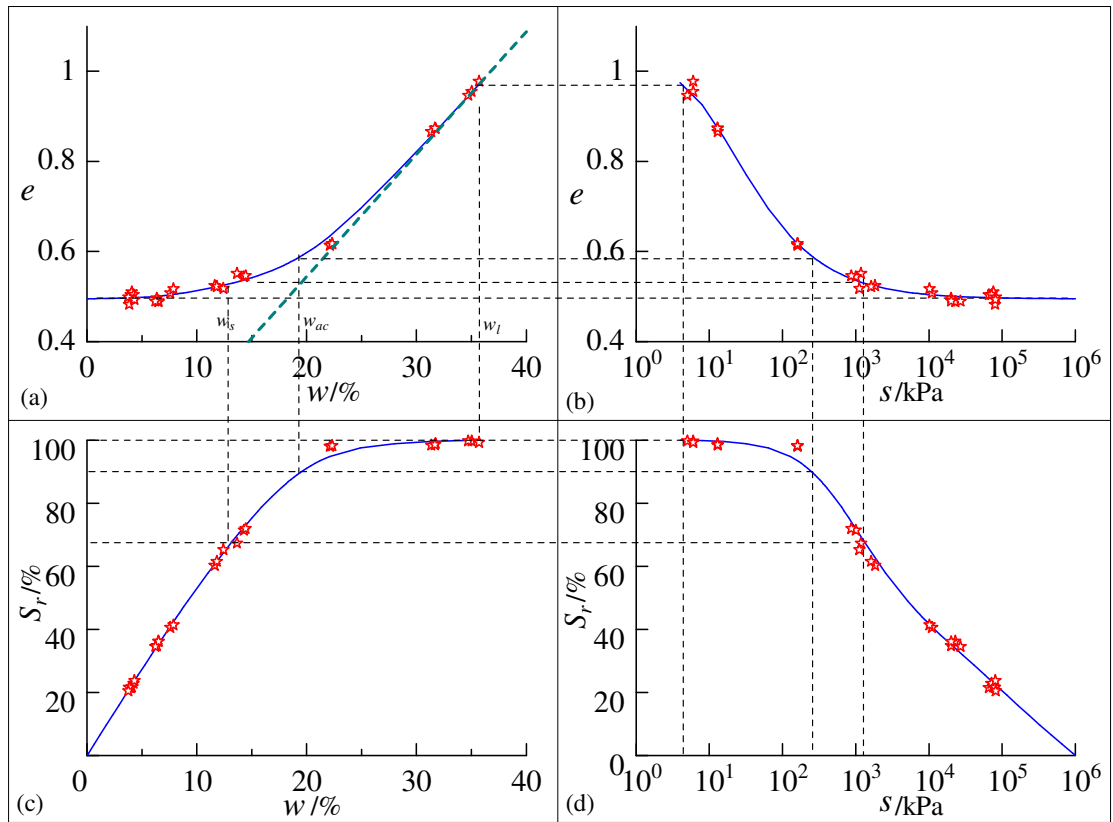
637

No.	Sample	s(kPa)	e	w(%)	S <sub>r</sub> (%)
	(1)-1	6	0.96	35.02	99.71
(1)	(1)-2	6	0.95	34.71	99.73
	(1)-3	5	0.98	35.70	99.28
	(2)-1	13	0.87	31.75	98.92
(2)	(2)-2	13	0.87	31.34	98.42
	(2)-3	13	0.87	31.68	98.58
	(3)-1	160	0.61	22.12	98.04
(3)	(3)-2	160	0.62	22.31	98.29
	(3)-3	160	0.62	22.31	98.24
	(4)-1	1000	0.54	14.29	71.42
(4)	(4)-2	1180	0.55	13.65	67.33
	(4)-3	870	0.55	14.44	71.92
	(5)-1	11020	0.51	7.58	40.61
(5)	(5)-2	10160	0.52	7.87	41.38
	(5)-3	20000	0.50	6.35	34.80
	(6)-1	65690	0.50	3.98	21.50
(6)	(6)-2	75610	0.51	4.07	21.70
	(6)-3	71510	0.50	4.24	22.89

638

639

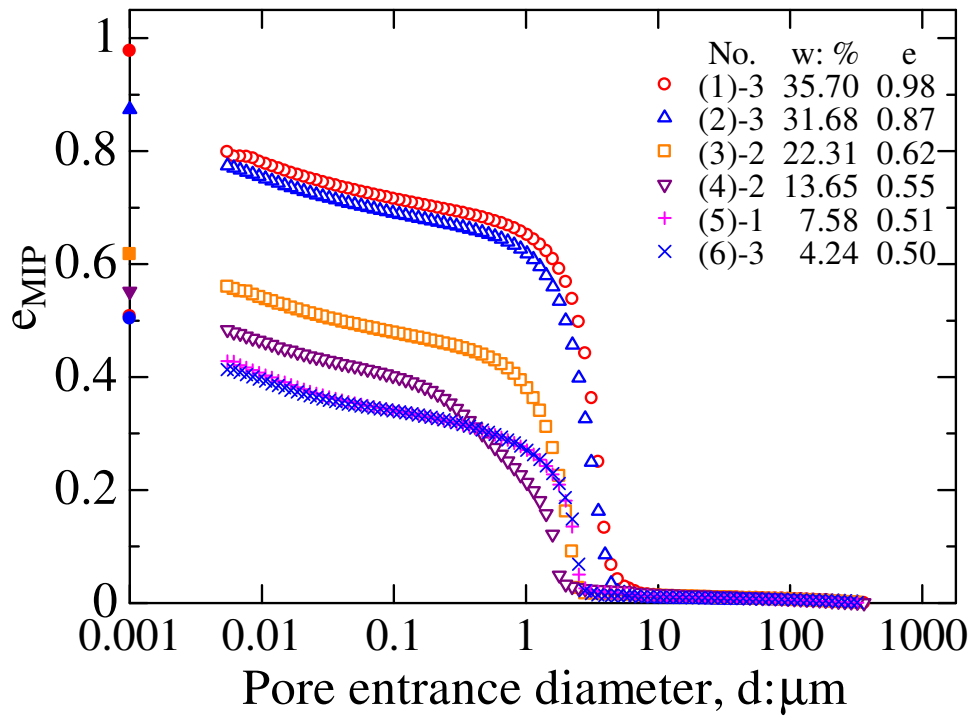
640 List of Figures



641

642 **Fig. 1** Results of the drying process of reconstituted Jossigny silt with  $w_i = 1.5 w_l$

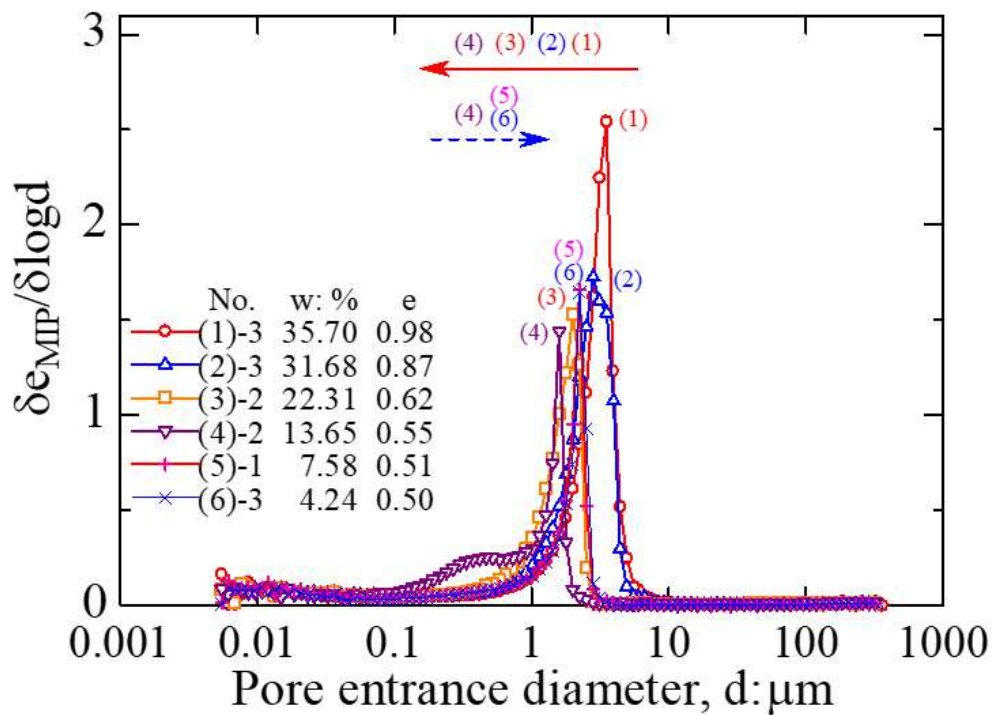
643



644

645

(a) Cumulative intrusion



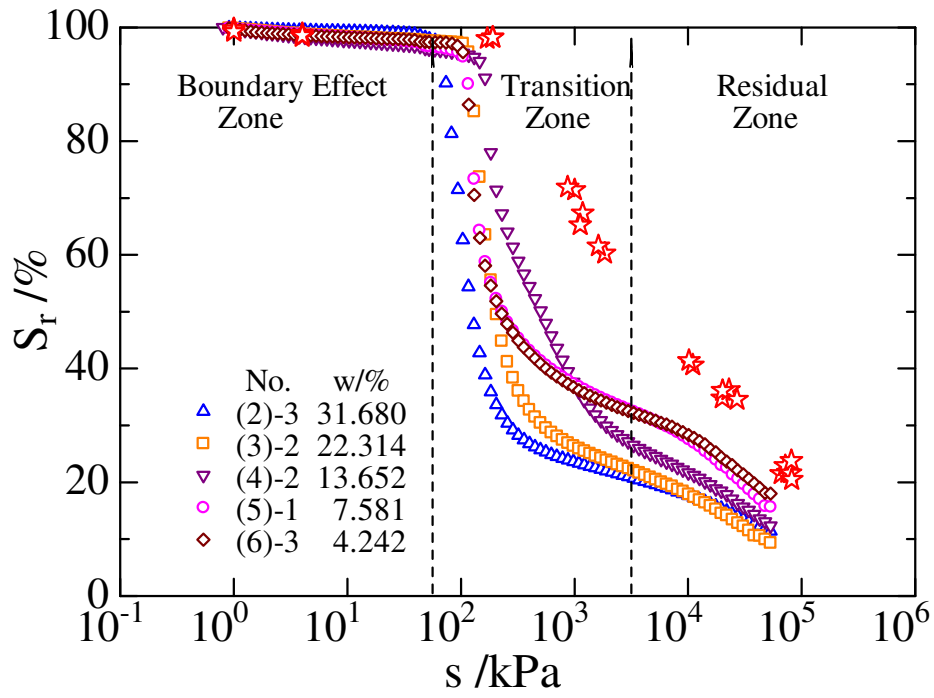
646

647

(b) PSD function

648 **Fig. 2** Pore size distribution of Jossigny silt during drying (data after Sun and Cui,

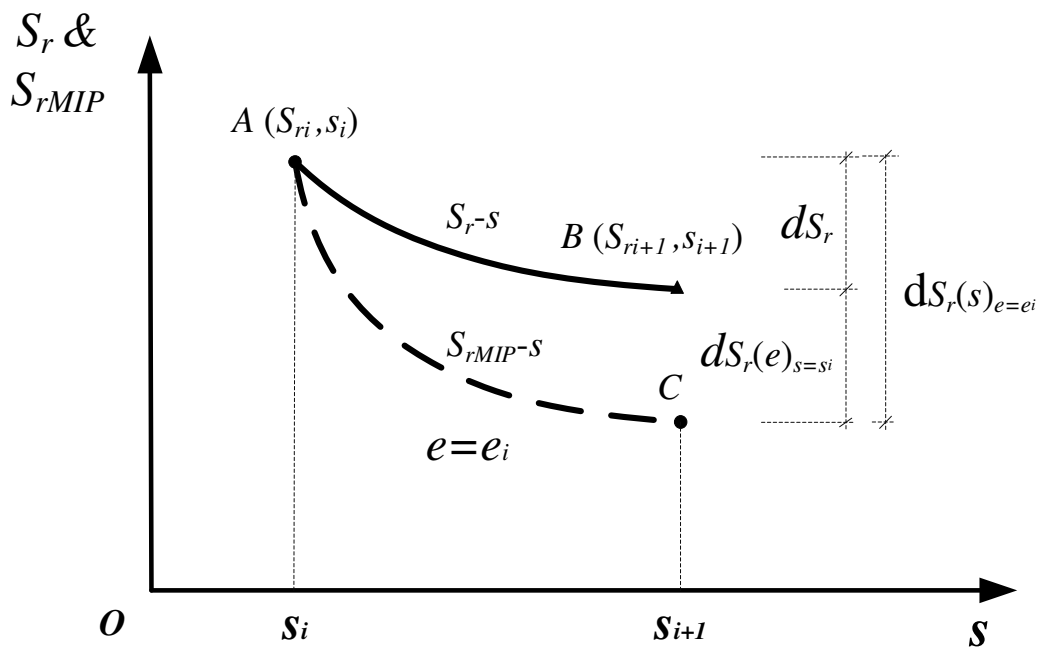
649 2018)



650

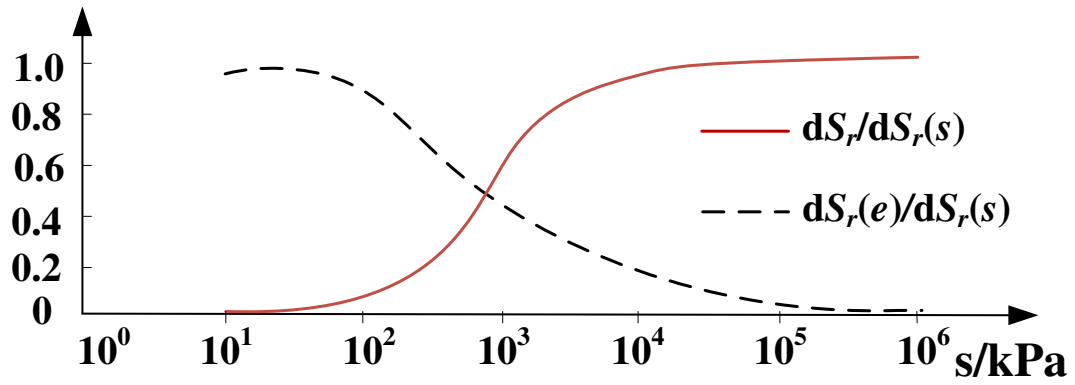
651 **Fig. 3**  $S_{rMIP}$ - $s$  relationships and  $S_r$ - $s$  relationship

652



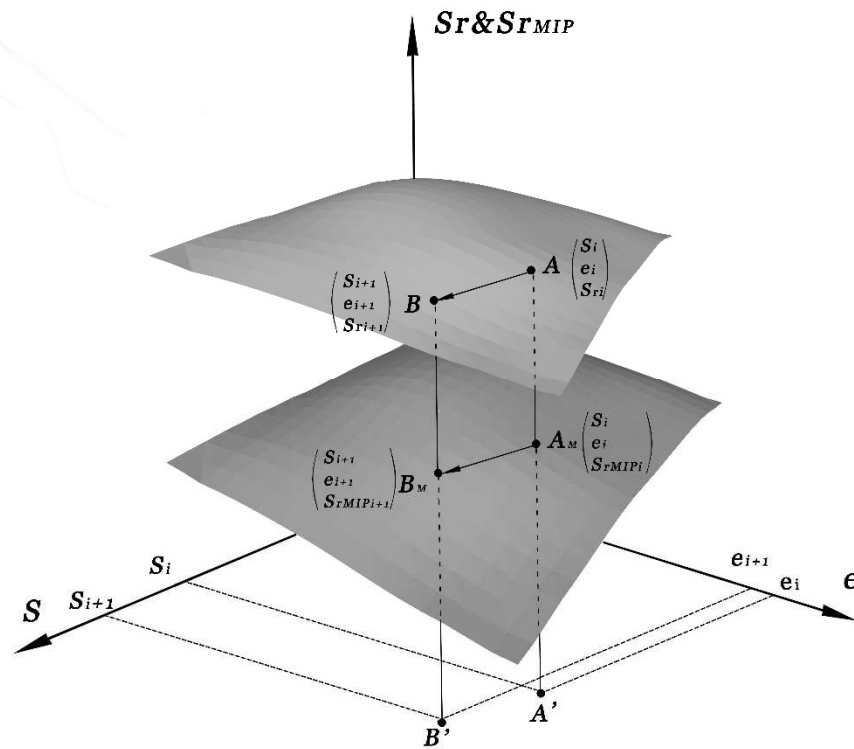
653

654 **Fig. 4**  $S_r$  ( $S_{rMIP}$ ) -  $s$  relationship



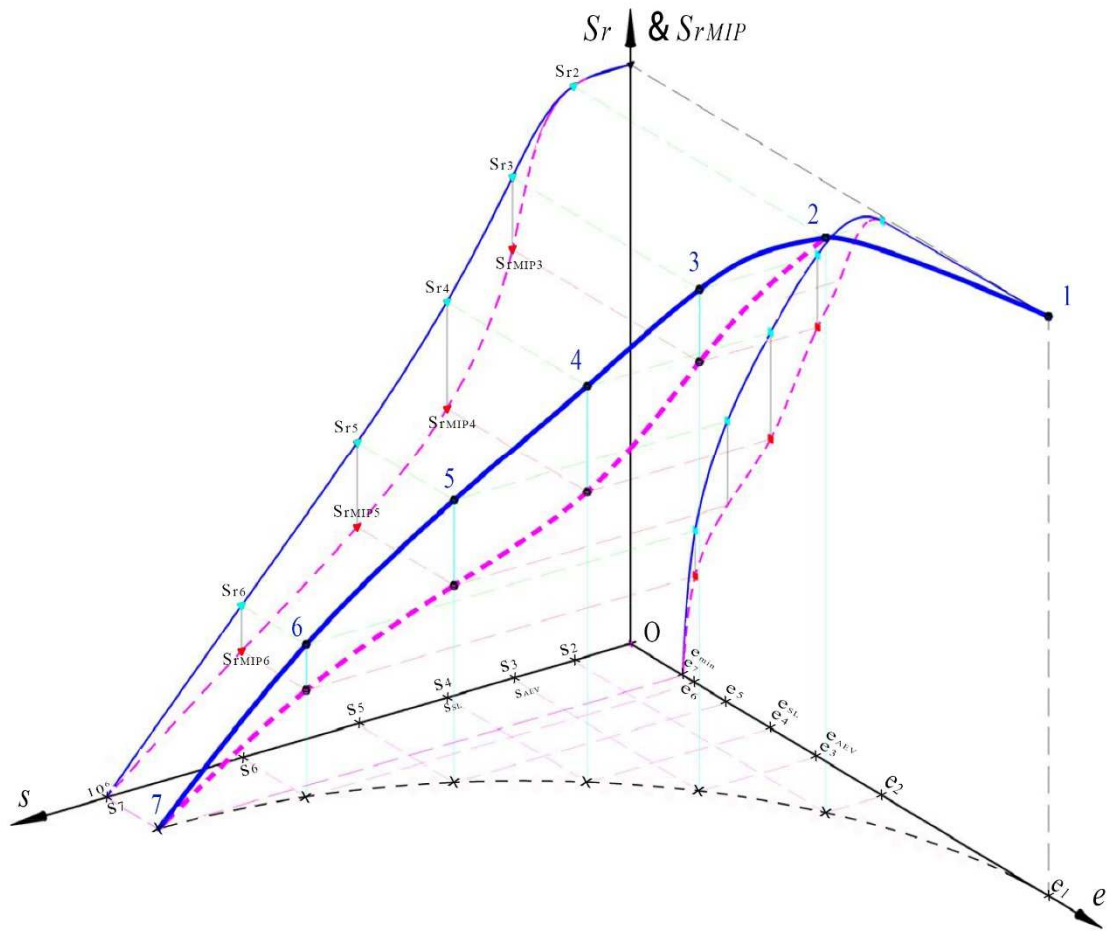
655

656 Fig. 5 Changes of  $dS_r(e)/dS_r(s)$  &  $dS_r/dS_r(s)$  with suction



657

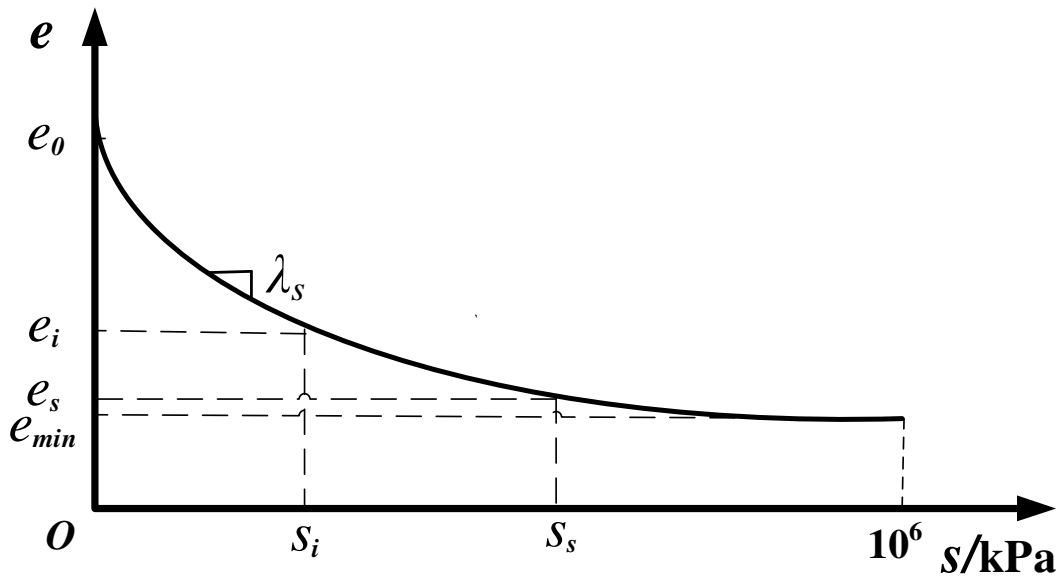
658 Fig. 6  $S_r(S_{rMIP})$ - $e$ - $s$  three-dimension diagram



659

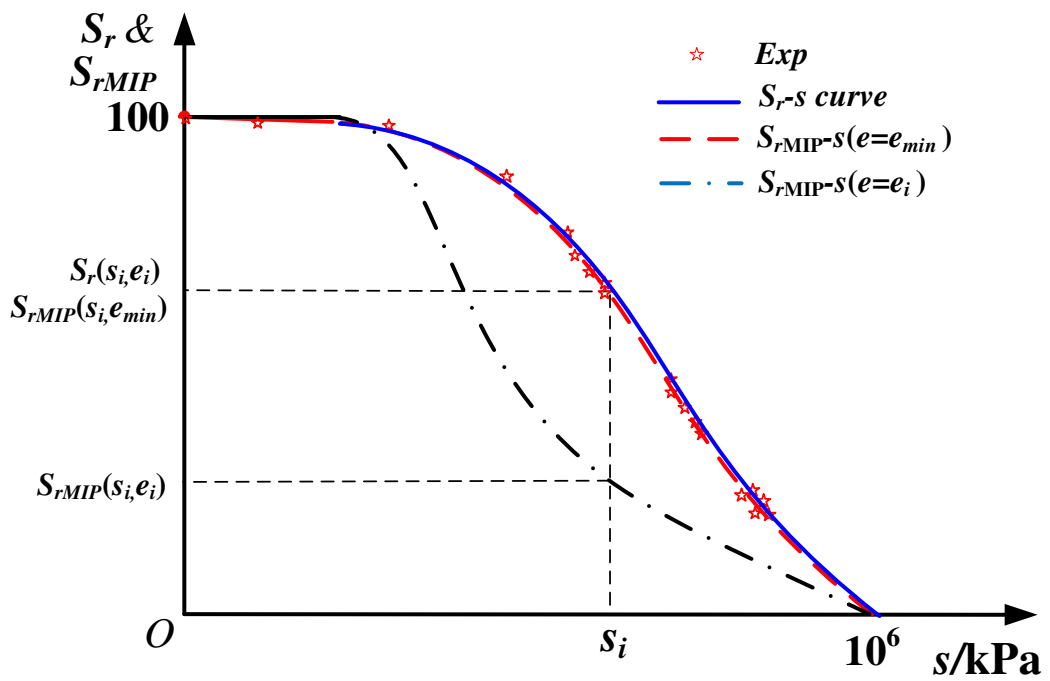
660 **Fig. 7** Projection of drying test results in  $S_r(S_{rMIP})$ - $e$ - $s$  three-dimension diagram

661



662

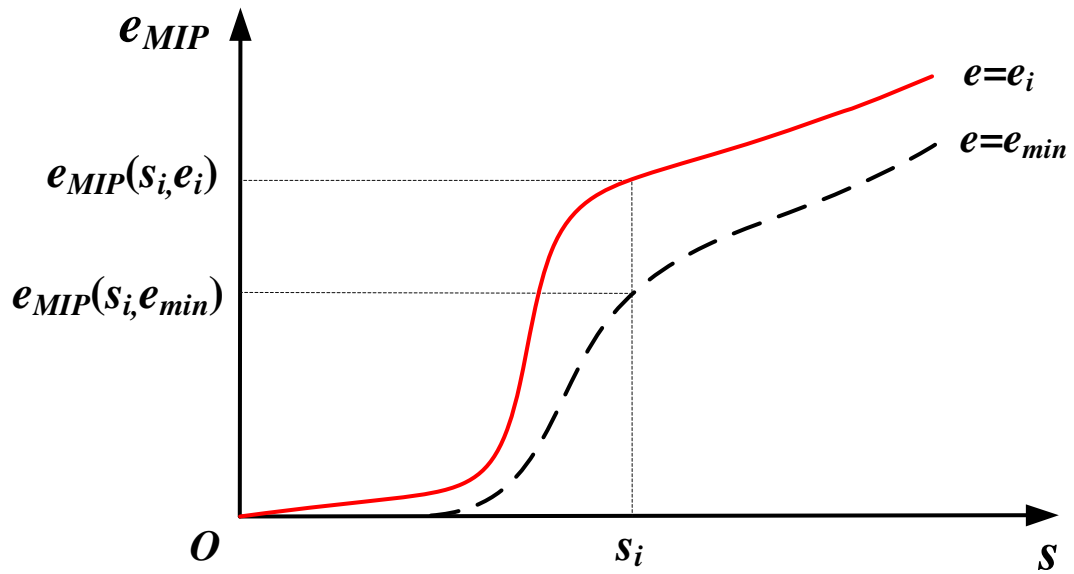
663 Fig. 8 e-s relationship



664

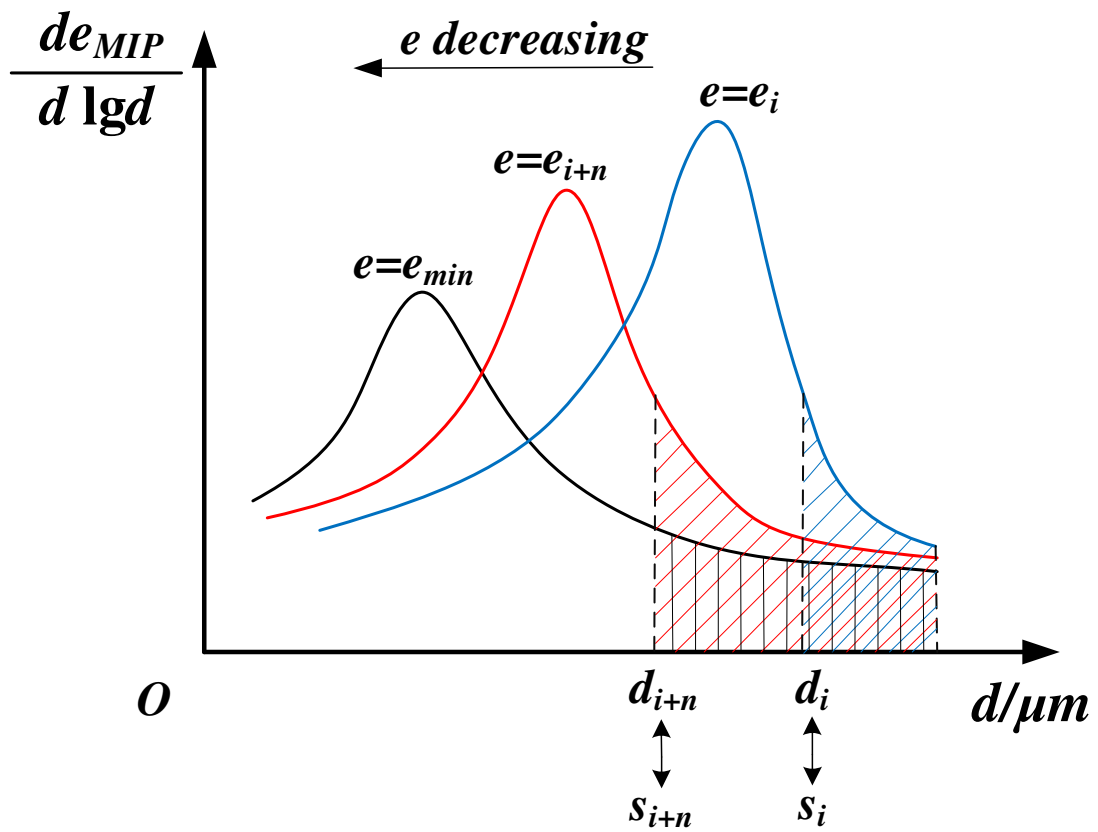
665 Fig. 9 Comparison and connection between  $S_{rMIP}$ - $s$  and  $S_r$ - $s$  relationship

666



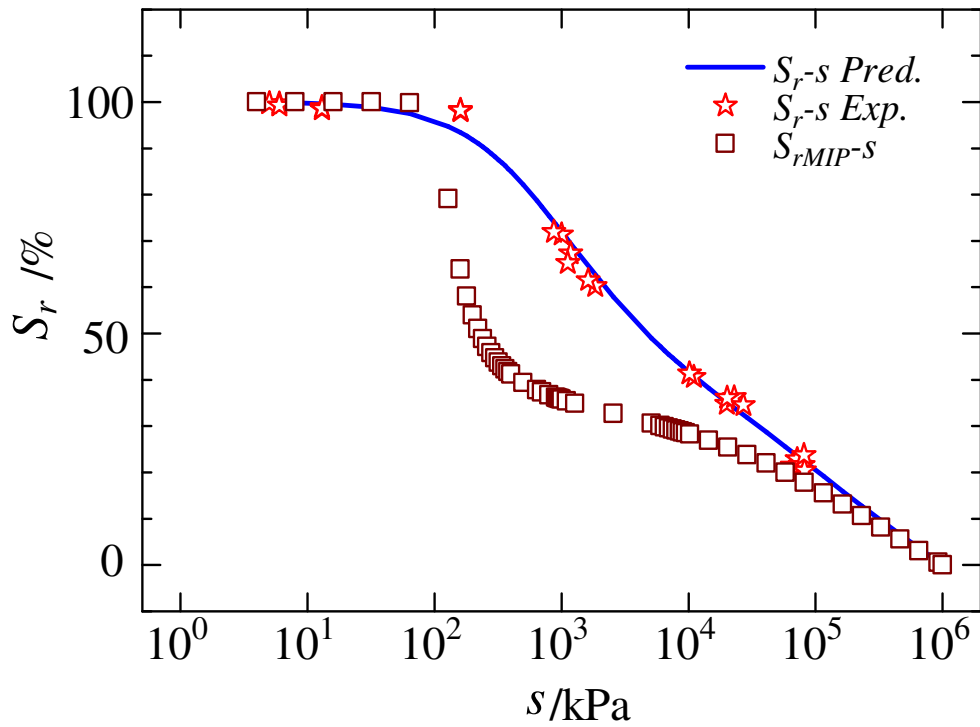
667

668 Fig. 10  $e_{MIP}$ - $s$  relationship



669

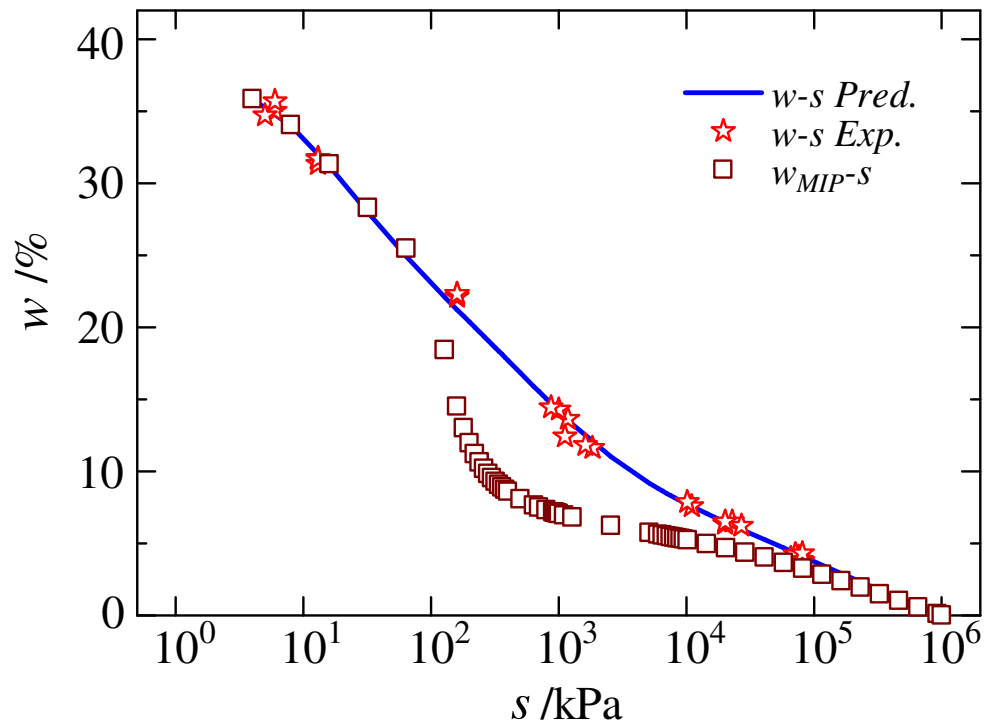
670 Fig. 11 Change of PSD function with void ratio decreasing from  $e=e_i$  to  $e_{min}$



671

672

(a)  $S_r$ - $s$



673

674

(b)  $w$ - $s$

675 **Fig. 12** Transformation of  $SWRC_{MIP}$  to conventional  $SWRC$  in drying of reconstituted

676 Jossigny silt